ROYAL SOCIETY
OF CHEMISTRY

COMMUNICATION

Check for updates

Tunable nano-interfaces between MnO_x and layered double hydroxides boost oxygen evolving electrocatalysis†

Yudong Xue, [id] abcd Zachary S. Fishman, [id] ac Jason A. Röhr, ac Zhenhua Pan, ac Yunting Wang, e Chunhui Zhang, e Shili Zheng, *b Yi Zhang b and Shu Hu [id] *ac

The development of low overpotential, non-precious metal oxide electrocatalysts is important for sustainable water oxidation using renewable energy. Here we report the fabrication of nano-interfaces between MnO_x nanoscale islands and NiFe layered double hydroxide (LDH) nanosheets, which were chosen as baseline electrocatalysts for OER activity tuning. The MnO_x nano-islands were grown on the surfaces of NiFe-LDH nanosheets by atomic layer deposition (ALD). Morphological and structural characterization indicated that the MnO_x formed flat nanoscale islands which uniformly covered the surfaces of NiFe-LDH nanosheets, giving rise to a large density of three-dimensional nano-interfaces at the NiFe-LDH/MnO_x/electrolyte multi-phase boundaries. We showed by X-ray spectroscopic characterization that these nano-interfaces induced electronic interactions between NiFe-LDH nanosheets and MnO_x nano-islands. Through such modifications, the Fermi level of the original NiFe-LDH was lowered by donating electrons to the MnO_x nano-islands, dramatically boosting the OER performance of these electron-deficient NiFe-LDH catalysts. Using only 10 cycles of ALD MnO_x, the MnO_x/NiFe-LDH nano-composites exhibited remarkable and enhanced electrocatalytic activity with an overpotential of 174 mV at 10 mA cm^{-2}. This work demonstrates a promising pathway for tuning transition metal electrocatalysts *via* a generic ALD surface modification technique.

1. Introduction

Currently, the interest in electrochemical oxygen evolution is growing for applications in efficient and sustainable energy conversion and storage, such as water splitting and metal–air batteries.[1–6] The oxygen evolution reaction (OER) concerns the electrical or photo-driven oxidation of water for producing molecular oxygen, and has been a major bottleneck in overall water splitting to generate H_2 fuels from sustainable energy sources.[7] The required overpotential at a given operating current density usually exceeds that for H_2 evolution.[8–11] Among the most efficient OER catalysts, precious metal oxides such as RuO_2 and IrO_2 suffer from element scarcity and high cost.[12] Alternatively, NiFe-based layered double hydroxides (LDHs), typical two-dimensional nanomaterials, exhibit outstanding OER activity compared to other mixed metal oxides, metal hydroxides, perovskites and noble metals in basic conditions.[13–15] Gong *et al.* decorated NiFe-LDH on carbon nanotube surfaces and achieved faster electron transfer rates and enhanced OER activity.[16] Zhou *et al.* introduced reducing flame treatments to NiFe-LDH surfaces to improve their OER performance by creating abundant surface oxygen vacancies.[17] However, those oxygen vacancies will likely be annihilated during the long-term operation of the electrocatalysts, especially under anodic conditions. Importantly, such surface modification is considered an emerging strategy for catalyst tuning to further improve the record activity of NiFe-LDH OER catalysts.[18]

In natural photosynthesis, manganese plays a vital role in the oxygen evolution in biological systems.[19] Nature uses three-dimensional structures of cubic Mn–O–Ca centres for oxygen evolution, whereas the structures of synthetic water-oxidation catalysts reported so far are mostly two dimensional such as inorganic NiFe-LDH sheets or di-valent metal centres with an oxo-bridge, and their active sites are not yet three-dimensional (3D).[20] Numerous studies have reported that manganese oxides including MnO, MnO_2, and Mn_2O_3 are effective OER catalysts.[21,22] MnO_x is susceptible to changing its surface oxidation state, which is beneficial for accepting or donating electrons during electrocatalysis.[23]

The above mentioned work has motivated investigation into atomic precision surface tuning by anchoring nanoscale MnO_x composites over two-dimensional NiFe-LDH nanosheets, to

aDepartment of Chemical and Environmental Engineering, Yale University, New Haven, Connecticut 06511, USA. E-mail: shu.hu@yale.edu; Tel: +1-203-737-6521

bNational Engineering Laboratory for Hydrometallurgical Cleaner Production Technology, Key Laboratory of Green Process and Engineering, Institute of Process Engineering, Chinese Academy of Sciences, Beijing 100190, China. E-mail: slzheng@ipe.ac.cn; Tel: +86-10-82544858

cEnergy Sciences Institute, Yale University, West Haven, Connecticut 06516, USA

dUniversity of Chinese Academy of Sciences, Beijing 100049, China

eSchool of Chemical and Environmental Engineering, China University of Mining and Technology (Beijing), Beijing 100083, China

achieve three-dimensional (3D) active sites formed on the LDH catalysts. However, traditional deposition methods for MnO_x, such as electrodeposition,[24] spray deposition,[25] and thermal decomposition[26] have difficulties in achieving deposition at the level of atomic precision. It is very difficult to fine tune the 3D structures of the active catalyst sites when using these processes and to achieve uniformity over nano-structured catalysts. For example, Jin et al. reported the superior catalytic performance of sub-10 nm-sized MnO_x nanocrystals that were monodispersed, partially oxidized, and fabricated by thermal decomposition, but it was difficult to precisely control their sizes at the nanometer or sub-nanometer level.[26] Besides, electrodeposited MnO_2 was reported to be a stable OER catalyst, but electrodeposition cannot easily achieve atomic scale control and tunability.[25]

Atomic layer deposition (ALD), owing to its capability for atomically precise control via surface-limited chemical growth, has attracted great attention for modifying surfaces and improving performance durability in broad applications including (photo-)catalysis, photovoltaics, and batteries.[27,28] Most reports about ALD oxide coatings are focused on corrosion protection or stabilization for water splitting (especially photoanodes).[29–33] As for tuning the electrocatalytic performance, constructing catalytically active sites by surface modification using ALD metal oxides is less investigated.

Herein, we have designed and fabricated OER electrocatalysts of MnO_x/NiFe-LDH nanocomposites by ALD MnO_x growth over NiFe-LDH nanosheets that were synthesized and immobilized onto Ni foams as conductive supports. The ALD-modified catalyst nanocomposites exhibited superb OER activity because of chemical bonding and atomic-scale anchoring of MnO_x nano-islands onto the nanosheet surfaces. Their crystal structures, surface morphology, elemental distribution, and oxidation states were systematically characterized using X-ray diffraction (XRD), scanning electron microscopy (SEM), transmission electron microscopy (TEM), energy dispersive X-ray spectroscopy (EDX), and X-ray photoelectron spectroscopy (XPS). Enhanced OER catalytic activity was observed and was attributed to the newly created 3D nano-interfaces of the MnO_x/NiFe-LDH nanocomposites, this promises a new class of practical energy conversion materials.

2. Experimental, synthesis and characterization

$Fe(NO_3)_3 \cdot 9H_2O$ (99.99%), $Ni(NO_3)_2 \cdot 6H_2O$ (99%), $Mn(NO_3)_2 \cdot 4H_2O$ (99%), and $CO(NH_2)_2$ (99.8%) were purchased from Sigma-Aldrich and were used as-received. Ni foam (99.8%, 1.5 mm thick) plates were purchased from Taiyuan Lizhiyuan Battery. Fluorine-doped tin oxide (FTO) substrates (TEC15) were purchased from Hartford Glass Co. All solutions were prepared using deionized water (18 MΩ cm) obtained from a Millipore deionized water system. The NiFe-LDH nanosheets were synthesized using a hydrothermal method and were directly deposited onto the Ni foam plates during the synthesis. 0.5 mmol $Ni(NO_3)_2 \cdot 6H_2O$, 0.5 mmol $Fe(NO_3)_3 \cdot 9H_2O$, and 5 mmol $CO(NH_2)_2$ were dissolved in 30 mL water. A Ni foam was

first cut into pieces at a size of 1 cm × 1.5 cm, and then subsequently cleaned with concentrated HCl (37% w/w), water, and ethanol with each step lasting for 5 min. The Ni foam was immediately transferred to a 50 mL autoclave which was maintained at 130 °C for 12 h. After cooling to room temperature, the electrode was washed with water and ethanol and subsequently dried in vacuo at 60 °C for 4 h. Following this procedure, NiFe-LDH nanosheets were uniformly grown on the Ni foam and inside its pores.

In order to construct MnO_x/LDH nano-interfaces and investigate their activity enhancement, MnO_x was deposited onto the LDH/Ni foam substrates by ALD from the top surface side. ALD growth of MnO_x was performed using an Ultratech Fiji G2a ALD system. Bis-(ethylcyclopentadienyl)manganese ($Mn(EtCp)_2$, Strem Chemicals, 98%) was used as the Mn precursor. The ALD chamber was set at 150 °C during growth. One MnO_x deposition cycle consisted of a 0.06 s pulse of H_2O, a 15 s pause, followed by two 0.25 s pulses of $Mn(EtCp)_2$ (the precursor temperature was held at 100 °C) spaced 7 s apart, and completed with another 0.06 s pulse of H_2O.[34,35] The total number of cycles was varied as 5, 10, 20, and 50 cycles, which was adjusted to target a series of coverages for the MnO_x modification. The FTO was also used as a MnO_x growth substrate for XPS characterization. For comparison, NiFeMn-LDH electrocatalysts were synthesized using a similar hydrothermal procedure to the NiFe-LDH synthesis by using 0.4 mmol $Ni(NO_3)_2 \cdot 6H_2O$, 0.4 mmol $Fe(NO_3)_3 \cdot 9H_2O$, 0.1 mmol $Mn(NO_3)_2 \cdot 4H_2O$, and 5 mmol $CO(NH_2)_2$ as the precursors.

Electrochemical measurements were performed using a Bio-Logic S200 potentiostat in a three-electrode cell. Cyclic voltammetry (CV) and linear sweep voltammetry (LSV), with a scan rate of 1 mV s^{-1}, were performed in 1 M KOH (aq) electrolyte. A carbon rod and a Hg/HgO electrode were used as the counter electrode and the reference electrode, respectively. The standard deviations of overpotentials were calculated by testing the electrodes 5 times. Electrochemical impedance spectroscopy (EIS) was performed in the same cell at an overpotential of 300 mV from 10^5 to 10^{-1} Hz. Stability testing was carried out using a chronopotentiometry technique at a current density of 10 mA cm^{-2}. A Hitachi SU8230 UHR Cold Field Emission SEM and a FEI Tecnai Osiris TEM were used to study the surface morphology and elemental distribution. XPS measurements were performed using a PHI Versa Probe II Scanning XPS Microprobe equipped with a monochromated Al source. The obtained data were analyzed using XPS Peak software. XRD patterns were collected using a Rigaku SmartLab X-ray diffractometer using a Cu Kα source. The faradaic efficiency of oxygen evolution on the MnO_x/LDH/Ni foam electrodes was quantified by comparing the amount of oxygen evolved to that of a standard Ir electrode.[34] The concentration of oxygen was measured using an oxygen probe (OX-NP, Unisense). Turnover frequency (TOF) values were calculated as follows:

$$TOF = \frac{jS}{4nF} \quad (1)$$

where j is the measured current density, S is the geometric area of the electrode, n is the number of moles of active materials

deposited on the working electrode based on the number of moles of all the metal species, and F is the Faraday constant (96 485 C mol^{-1}).[36,37] The metal ratio of LDH on Ni foam was determined using inductively coupled plasma-mass spectrometry (ICP-MS, Model iCAP Qc, Thermo Scientific) by exfoliating the LDH nanomaterials from the electrode carefully. The number of moles of active materials on the Ni foam was calculated from the Fe molar amount and the Ni/Fe ratio.

3. Results and discussion

To test the electrocatalytic behaviour, a 3D MnO$_x$/NiFe-LDH nanocomposite electrode was prepared *via* a two-step "bottom-up" approach consisting of a hydrothermal synthesis process and a subsequent ALD modification process. Specifically, the NiFe-LDH nanosheet arrays were first grown on a Ni foam substrate and then decorated with nano-islands of MnO$_x$ by ALD synthesis. MnO$_x$ was chemically grown on NiFe-LDH surfaces by using Mn(EtCp)$_2$ as the Mn precursor and H$_2$O as the co-reactant. Fig. S1 and S2† illustrate the ALD process, which consisted of successive self-limiting surface reactions between the precursor (Mn(EtCp)$_2$) vapors and H$_2$O over the NiFe-LDH substrate. At the molecular level, the surface reactions during Mn(EtCp)$_2$ exposure are given by eqn (2).[35] Here * refers to surface reactive species.

$$Ni(Fe)OH^* + Mn(EtCp)_2 \rightarrow Ni(Fe)O\text{--}MnEtCp^* + H^+[EtCp]^- \tag{2}$$

Mn(EtCp)$_2$ can react with surface hydroxyl groups and releases a complex of protons (possibly attached to H$_2$O molecules) and EtCp anions as a product, *i.e.* H$^+$[EtCp]$^-$. The subsequent surface reactions during H$_2$O exposure are given by eqn (3) and (4).[35]

$$Ni(Fe)O\text{--}MnEtCp^* + H_2O \rightarrow Ni(Fe)O\text{--}Mn\text{--}OH^* + H^+[EtCp]^- \tag{3}$$

$$MnOH^* + Mn(EtCp)_2 \rightarrow MnO\text{--}MnEtCp^* + H^+[EtCp]^- \tag{4}$$

H$_2$O can react with a surface MnEtCp* resulting in a hydroxyl-terminated surface, after which MnO$_x$ will complete its deposition on the substrate. In the first cycle, Mn(EtCp)$_2$ will react with surface hydroxyl groups on the NiFe-LDH substrate to produce a certain number of nucleation sites. In the following ALD cycles, the growth of MnO$_x$ is continued on these MnO$_x$ sites to generate partially covered structures of MnO$_x$ nano-islands on LDH nanosheet surfaces, as indicated in eqn (4). Unreacted precursor molecules, along with volatile products, were removed in a continuous flow of inert Ar gas. The crystal structures of the as-prepared samples with varying ALD MnO$_x$ cycles (from 5 to 50) were determined using XRD, as shown in Fig. 1. Three evident diffraction peaks, located at 44.3°, 51.8°, and 76.5°, corresponded to the (111), (200), and (220) crystal planes of the Ni foam substrates (PDF no. 70-0989), respectively. Prior to the ALD process, the NiFe-LDH samples generated XRD patterns with diffraction peaks at 11.35°, 22.74°, 34.41°, 38.77°,
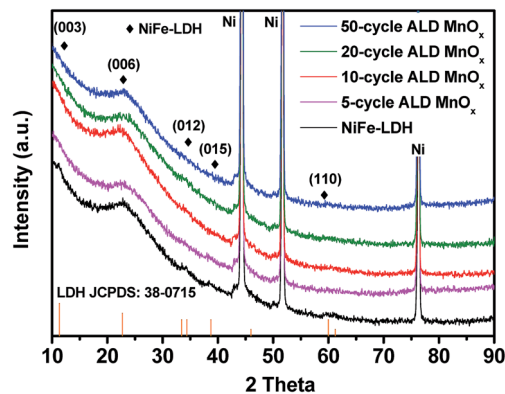

Fig. 1 XRD patterns of NiFe-LDH and with 5 cycles, 10 cycles, 20 cycles, and 50 cycles of ALD MnO$_x$ grown over NiFe-LDH catalysts.

and 59.98°, which were assigned to the (003), (006), (012), (015), and (110) crystal planes of layered NiFe-LDH.[38] The peak intensity of LDH was relatively weak, which is mainly caused by the overshadowing effect of the Ni foam substrates.[39] After the ALD process, no additional diffraction peaks were introduced. In fact, the intensity of most NiFe-LDH peaks decreased slightly because the surface-deposited amorphous MnO$_x$ reduced the ordering of the crystal planes of the NiFe-LDH apart from the (006) planes. By analyzing all the diffraction peaks of NiFe-LDH with varying ALD MnO$_x$ cycles, it was concluded that the predominant NiFe-LDH phase was either of low crystallinity or amorphous. Regarding the structure of the MnO$_x$ surface modification, a few layers of Mn–O octahedral clusters that are aggregated in a flat nano-island shape should be a good representation: these nano-islands covered the surfaces of NiFe-LDH nanosheets uniformly throughout the electrode surfaces, and were in contact with liquid electrolytes during catalyst operation.

The OER performance of the as-grown NiFe-LDH and MnO$_x$/NiFe-LDHs was evaluated in 1 M KOH (aq) electrolyte by cyclic voltammetry. As shown in Fig. 2a, the overpotentials at a current density of 10 mA cm^{-2} were measured to be 216, 192, 174, 178, and 199 mV for the 0, 5, 10, 20, and 50 cycles of ALD MnO$_x$, respectively. The standard deviations of the measured overpotentials were ±10 mV. In comparison to the original NiFe-LDH, the OER activity can be enhanced by ALD MnO$_x$ modification in varying degrees but with slight differences. Among them, the 10 cycles of ALD MnO$_x$/LDH exhibited the best OER performance, and its pre-catalytic redox wave showed the largest anodic shift which is consistent with the strong electronic interactions reported for Co–Fe systems.[40] To achieve a catalytic current density of 50 mA cm^{-2}, an overpotential of 283 mV only was needed for the 10 cycles of MnO$_x$/LDH, which is much lower than that of the original LDH (357 mV). The NiFeMn-LDH electrocatalysts were nanosheet structures consisting of homogeneously distributed Ni, Fe, and Mn without over-coated MnO$_x$ islands. They also showed improved OER activity with the introduction of Mn into the LDH nanomaterials. However, their activity was lower than that of ALD MnO$_x$-modified samples that feature the engineered MnO$_x$/

Fig. 2 The cyclic voltammetry curves (a) and Tafel plots (b) of ALD MnO_x/NiFe-LDH electrodes measured in 1 M KOH (aq) at a scan rate of 1 mV s^{-1}.

NiFe-LDH interfaces. Additionally, we compared the electrochemical kinetics of the ALD samples with the original NiFe-LDH using a Tafel plot as shown in Fig. 2b. The Tafel slope of the 10 cycles of MnO_x/NiFe-LDH sample (48 mV dec^{-1}) was smaller than that of the original NiFe-LDH (65 mV dec^{-1}) without the MnO_x modification. This comparison illustrates that the MnO_x-modified nanocomposites favored faster kinetics with a reduced Tafel slope and possibly with a shift in the catalytic mechanism. The Tafel slope provides important information about the rate determining step (RDS) of four-electron/four-proton OER reactions. The corresponding Tafel slope of the second-electron-transfer limited mechanism would be between 70 mV dec^{-1} and 30 mV dec^{-1} if the second electron-transfer step of chemical O–O coupling and the resulting *OOH formation was the RDS,[41] whereas the Tafel slope of the third-electron-transfer limited mechanism would be 30 mV dec^{-1}. Hence, the change in the Tafel slope from 65 to 48 mV dec^{-1} for the MnO_x modified sample suggests a changing trend for the RDS from predominately the second electron-transfer step to the third electron-transfer step of *OOH deprotonation and O_2 release upon MnO_x modification.[41] This mechanistic shift is a definitive sign of the ALD modifications improving electrocatalytic activity. Therefore, 10 cycles of ALD MnO_x/NiFe-LDH was considered as the representative OER electrode for further materials characterization and spectroscopic analysis.

Fig. 3 shows SEM images of the 10 cycles of ALD MnO_x grown on top of the NiFe-LDH nanosheets. The nanosheet structure of modified NiFe-LDH (Fig. 3a and b) was well-retained from its original morphology (Fig. 3c and d). For such highly non-uniform and non-planar surfaces of NiFe-LDH, the exceptional uniformity by the ALD coating is well demonstrated: nanometer-scale MnO_x islands were observed to cover the surfaces of LDH sheets, as shown in Fig. 3b, but not to replace surface Ni or Fe cations. Furthermore, TEM was employed to characterize the nanoscale heterostructured interfaces, for example, by using fragments of the MnO_x/LDH samples (exfoliated from the electrode carefully) (shown in Fig. 4a). The high-resolution TEM images showed lattice fringes with an interplanar spacing of 0.25 nm corresponding to the spacing of the (012) crystal planes of NiFe-LDH.[16] Amorphous MnO_x nano-islands were uniformly grown on the nanosheets (Fig. 4b). To further evaluate the morphology and the composition of the as-fabricated electrode materials, a HAADF-STEM mode with energy-dispersive X-ray spectroscopy (EDX) was employed. The areal average of the EDX composition mapping gave 8% Mn in atomic percentage on the NiFe-LDH sample surface (Fig. 4c). As shown in the EDX elemental mapping (Fig. 4d), the majority of Ni, Fe, and O was uniformly distributed within the nanosheets, while islands of Mn were distributed over the NiFe-LDH surface randomly but with a homogenous distribution. This observation indicated that the nano-interfaces of MnO_x/NiFe-LDH heterostructures were successfully constructed. The heterostructured MnO_x/NiFe-LDH nano-interfaces created a large amount of edge sites, which were identified as one of the major reasons for the boosted OER activity of the electrodes (see discussion below). The partially covered LDH catalysts consist of exposed edge sites at MnO_x/NiFe-LDH nano-interfaces, which operate synergistically for OER, side-by-side with the original and uncovered NiFe-LDH catalytic sites.

To understand the electronic interactions between MnO_x and NiFe-LDH, the elemental composition and valence states of the 10-cycle ALD MnO_x/NiFe-LDH sample were investigated by XPS. The XPS survey spectrum confirmed the presence of Ni, Fe, O, and Mn on the sample surface (Fig. S4†). The XPS spectrum of the Mn $2p_{3/2}$ core-level photoemission was deconvoluted by six Gaussian peaks following our previously published work as shown in Fig. 5a, and the binding energies of the respective peaks are listed in Table S1.†[34] In order to determine the valence state of Mn, pure ALD MnO_x was used for comparison. The fitting results indicated that Mn in MnO_x was predominantly +2 in valency for both ALD MnO_x and MnO_x/LDH nanocomposites. Furthermore, when MnO_x islands were deposited on NiFe-LDH, a small positive shift in the position of the Mn $2p_{3/2}$ signal intensity maximum was observed (from 641.9 to 642.0 eV) and the fitted peak (peak 1 labelled by a black arrow) at a binding energy of 640.2 eV increased in intensity as compared to ALD MnO_x (Fig. 5a). Both observations indicated that MnO_x received electrons and became electron-rich. In other words, MnO_x filled its empty states showing a raised Fermi level as evidenced by a slight increase of Mn $2p_{3/2}$ core-level binding energies.

Accordingly, we would expect a depletion of surface electrons for NiFe-LDH nanosheets, which would be evidenced by

Fig. 3 (a) and (b) SEM images of 10-cycle ALD MnO_x nano-islands grown on NiFe-LDH nanosheets, and (c) and (d) the original NiFe-LDH without modification.

a decrease in binding energies in the Ni $2p_{3/2}$ and Fe $2p_{3/2}$ XPS core-level spectra after MnO_x modification. In other words, the Ni or Fe core-level binding energy, *i.e.* the energy-level difference spanning from the NiFe-LDH Fermi level to the core level of Ni or Fe cations, would be reduced. A similar energy-level analysis by photoelectron spectroscopy has been described previously.[42] The XPS spectra of the Ni $2p_{3/2}$ and Fe $2p_{3/2}$ photoemissions were curve-fitted as shown in Fig. 5b and c. The binding energies of 856.0 and 713.0 eV for the MnO_x/NiFe-LDH composite were attributed to the Ni^{2+} and Fe^{3+}, respectively.[13,43] These valence states are in good agreement with those measured for the original NiFe-LDH. The Fermi level of NiFe-LDH nanosheets was found to be modified by MnO_x overlayers: the binding energies of Ni $2p_{3/2}$ and Fe $2p_{3/2}$ peak positions in MnO_x-modified NiFe-LDH (856.0 eV and 713.0 eV) were lower than those of the original NiFe-LDH (856.8 eV and 715.0 eV). This electron depletion at NiFe-LDH surfaces was indicative of covalent coordination and electronic interaction between NiFe-LDH nanosheets and ALD-overgrown MnO_x. Therefore, it confirmed the tuning of NiFe-LDH electronic properties by anchoring MnO_x nano-islands on catalyst surfaces.

To further understand the electrochemical performance of MnO_x/NiFe-LDH nanocomposites, TOF, electrochemical impedance, Faradaic efficiency, and long-term durability were quantified. The molar amounts of metals in these samples were determined by ICP-MS and are listed in Table S3.† Based on eqn (1), the lower limits of TOF for MnO_x/LDH and NiFe-LDH at a 300 mV overpotential were 0.0066 and 0.0043 s^{-1} as shown in Table S4,† demonstrating that the intrinsic OER activity of

MnO_x/LDH active sites was better than that of the original NiFe-LDH without modification. EIS analysis indicated that MnO_x/LDH nanocomposites had a lower charge-transfer resistance (R_{ct}, 5.89 Ω) than the original LDH (8.13 Ω) as shown in Fig. S3,† suggesting a faster electron transfer process during OER. Moreover, the quantity of oxygen accumulated at 10 mA cm^{-2} based on MnO_x/NiFe-LDH nanocomposites matched with the calculated amount for OER assuming a faradaic efficiency of ∼100% as shown in Fig. 5d. Long-term performance stability during OER is important for practical applications. Chronopotentiometry measurements showed excellent stability of the NiFe-LDH as the catalysts operated at a constant current density of 10 mA cm^{-2} for 10 h, comparable to that of the original NiFe-LDH.[8,13] Only a 6 mV increase in the overpotential was observed during 10 h of operation, which affirmed the structural and functional stability of the covalent bonding between ALD MnO_x and NiFe-LDH nanosheets. According to the SEM image of the 10-cycle ALD MnO_x/NiFe-LDH electrode after long-term electrocatalysis (Fig. S5†), the nanosheet morphology was maintained, suggesting excellent structural stability. Additionally, the composition analysis of the electrode material after 10 h of stability testing as determined by ICP-MS (Table S3†) revealed that the ratios of Ni/Fe/Mn metals or the Mn composition in the MnO_x/NiFe-LDH samples were close to the values before long-term electrocatalysis. These results indicate that the active site structures of MnO_x were well preserved after 10 h of operation. Furthermore, XPS was also employed to evaluate the chemical stability of the MnO_x/LDH surface after the 10 h operation. The valence states of MnO_x nano-islands after OER
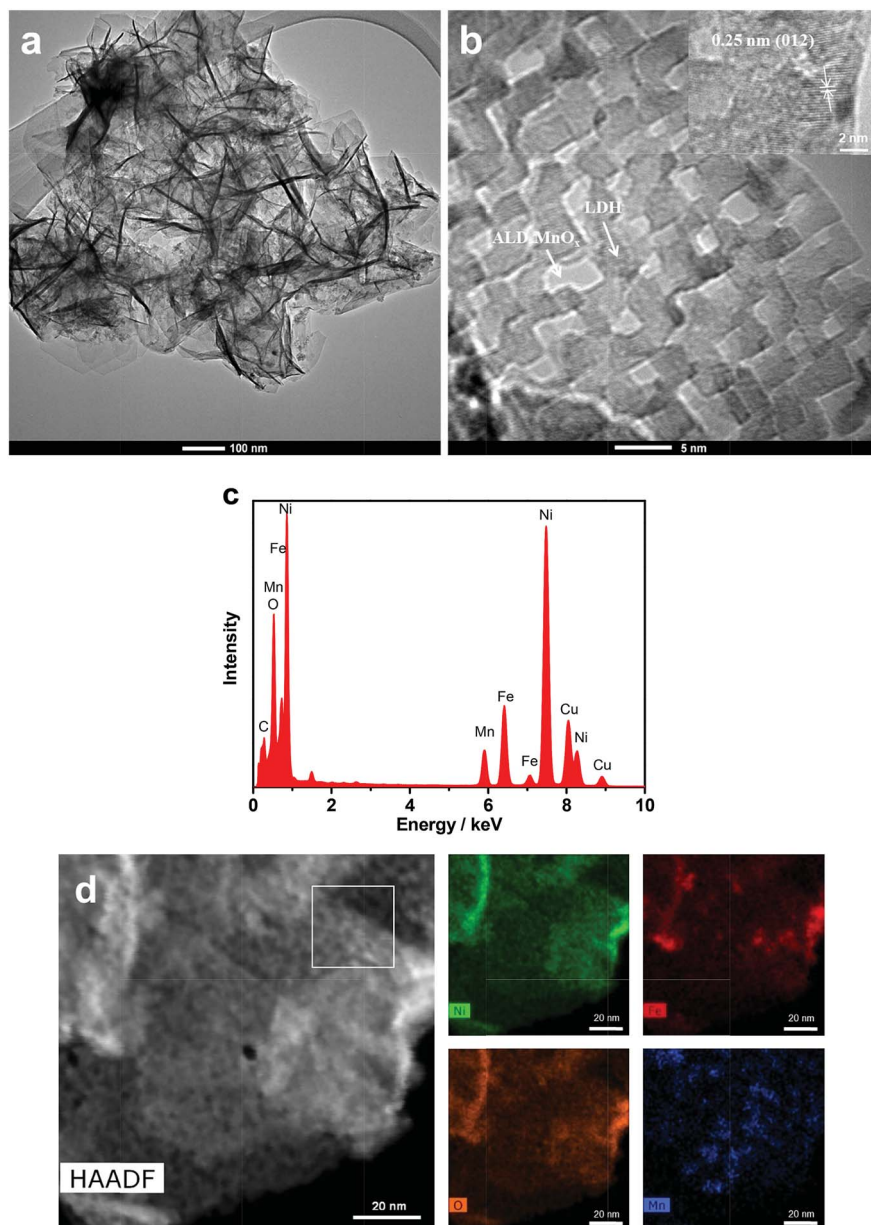
Fig. 4 TEM bright-field micrograph (a), high-resolution (HRTEM) micrograph (b), EDX (c), and HAADF-STEM image and EDX elemental mapping of 10-cycle MnO_x/LDH (d). The white box in (d) indicates the selected region for the HRTEM micrograph in (b).

showed no obvious change (Fig. 4a), which indicated the chemical stability of the Mn^{2+} cations during long-term OER operation. This is also consistent with the reported electrochemical performance stability.

As for the mechanism of improved OER activity, both the structural effects and electronic tuning of 3D MnO_x/NiFe-LDH nano-interfaces are considered to contribute. *Ab initio* calculations and *in situ* spectroscopic measurements reported that the original NiFe-LDH systems featured cooperation between Fe(IV) (which first stabilizes O radicals) and Ni(IV) (which then catalyzes chemical O–O coupling).[15,41] Exchange interactions between di-valent metal centres, *e.g.* neighboring Ni and Fe cations, were recently considered, which suggested that the delocalization of electron spins from high spin Fe^{4+} centres

reduced the free energy cost for the O–O coupling RDS. After MnO_x deposition and modification, the spin correlation between $Mn(II)O_x$ with a high spin d^5 configuration and Ni–Fe centres may further reduce the activation barrier for the O–O coupling RDS, which is consistent with the reduced Tafel slope from 65 mV dec^{-1} to 48 mV dec^{-1}. In this case, atomically precise MnO_x modification created a large number of active edge sites at the MnO_x/NiFe-LDH nano-interfaces. The enhancement of MnO_x-induced edge sites outperformed the original Ni and Fe active sites covered by MnO_x nano-islands. The MnO_x nano-islands induced electronic tuning of the original NiFe-LDH nanosheets. Furthermore, the structural environment at the newly introduced edge sites by MnO_x/NiFe-LDH nanocomposites could stabilize reaction intermediates and

This journal is © The Royal Society of Chemistry 2018

J. Mater. Chem. A, 2018, **6**, 21918–21926 | **21923**

Fig. 5 XPS spectra of Mn 2p$_{3/2}$ (a), Ni 2p$_{3/2}$ (b) and Fe 2p$_{3/2}$ (c) core-level photoemissions for the 10-cycle MnO$_x$/LDH (before and after OER testing) and original NiFe-LDH samples. Peak 1 of each spectra fitting is labelled with a black arrow in (a). (d) Generated O$_2$ gas molar quantities as a function of time overlaid with the calculated quantities of evolved O$_2$ assuming 100% faradaic efficiency. (e) Chronopotentiometric measurements recorded for 10-cycle MnO$_x$/LDH electrocatalysts at a constant current density of 10 mA cm^{-2}.

enhance the oxidative activity of NiFe-LDH.[44] Therefore, the above analysis clearly suggests the advantage of both the structural and the electronic tuning *via* MnO$_x$/LDH nanocomposites for boosting the OER activity. As the structure and valence state of MnO$_x$ nano-islands persevered as shown by characterization after stability testing, these 3D nano-interfaces promise long-lasting improvements to OER activity.

4. Conclusions

In summary, heterostructures of MnO$_x$/NiFe-LDH nanocomposites were successfully fabricated and finely tuned by few-cycle atomic layer deposition (ALD) over hydrothermally grown NiFe-LDH oxygen evolving catalysts. The MnO$_x$ nano-islands were uniformly anchored on the LDH support, creating a high density of functional nano-interfaces. The 3D engineering of MnO$_x$/LDH nano-interfaces resulted in electronic tuning of NiFe-LDH catalytic sites on the nanosheets, and additionally introduced new active sites at the edges of the MnO$_x$ nano-islands, outperforming that of the original NiFe-LDH. The optimized combination of 10-cycle ALD MnO$_x$/NiFe-LDH nanosheets showed the highest OER activity, affording a current density of 10 mA cm^{-2} at a small overpotential of 174 mV, a Tafel slope as small as 48 mV dec^{-1}, and 10 hour

stability in alkaline media. The presented surface modification not only provides a promising pathway towards efficient non-precious metal oxide OER electrocatalysts, but also offers insights into the construction of new types of electrocatalytic active site, such as ALD-grown 3D nano-interfaces, on energy converting materials.

Conflicts of interest

There are no conflicts to declare.

Acknowledgements

References

1 J. Luo, J. H. Im, M. T. Mayer, M. Schreier, M. K. Nazeeruddin, N. G. Park, S. D. Tilley, H. J. Fan and M. Gratzel, *Science*, 2014, **345**, 1593–1596.

2 Q. Li, D. Wang, C. Han, X. Ma, Q. Lu, Z. Xing and X. Yang, *J. Mater. Chem. A*, 2018, **6**, 8233–8237.

3 B. M. Hunter, H. B. Gray and A. M. Muller, *Chem. Rev.*, 2016, **116**, 14120–14136.

4 L. Yu, J. F. Yang, B. Y. Guan, Y. Lu and X. W. D. Lou, *Angew. Chem., Int. Ed.*, 2018, **57**, 172–176.

5 J. Tian, J. Chen, J. Liu, Q. Tian and P. Chen, *Nano Energy*, 2018, **48**, 284–291.

6 Z. W. Seh, J. Kibsgaard, C. F. Dickens, I. Chorkendorff, J. K. Nørskov and T. F. Jaramillo, *Science*, 2017, **355**, eaad4998.

7 N. T. Suen, S. F. Hung, Q. Quan, N. Zhang, Y. J. Xu and H. M. Chen, *Chem. Soc. Rev.*, 2017, **46**, 337–365.

8 S. Jung, C. C. L. McCrory, I. M. Ferrer, J. C. Peters and T. F. Jaramillo, *J. Mater. Chem. A*, 2016, **4**, 3068–3076.

9 J. Nai, Y. Lu and X.-Y. Yu, *J. Mater. Chem. A*, 2018, DOI: 10.1039/c8ta02334d.

10 X. Zhao, F. Li, R. Wang, J.-M. Seo, H.-J. Choi, S.-M. Jung, J. Mahmood, I.-Y. Jeon and J.-B. Baek, *Adv. Funct. Mater.*, 2017, **27**, 1605717.

11 Y. Zhou, S. Sun, J. Song, S. Xi, B. Chen, Y. Du, A. C. Fisher, F. Cheng, X. Wang, H. Zhang and Z. J. Xu, *Adv. Mater.*, 2018, **30**, e1802912.

12 W. Xu, F. Lyu, Y. Bai, A. Gao, J. Feng, Z. Cai and Y. Yin, *Nano Energy*, 2018, **43**, 110–116.

13 Z. Lu, W. Xu, W. Zhu, Q. Yang, X. Lei, J. Liu, Y. Li, X. Sun and X. Duan, *Chem. Commun.*, 2014, **50**, 6479–6482.

14 H. Yin and Z. Tang, *Chem. Soc. Rev.*, 2016, **45**, 4873–4891.

15 B. M. Hunter, N. B. Thompson, A. M. Müller, G. R. Rossman, M. G. Hill, J. R. Winkler and H. B. Gray, *Joule*, 2018, **2**, 747–763.

16 M. Gong, Y. Li, H. Wang, Y. Liang, J. Z. Wu, J. Zhou, J. Wang, T. Regier, F. Wei and H. Dai, *J. Am. Chem. Soc.*, 2013, **135**, 8452–8455.

17 D. Zhou, X. Xiong, Z. Cai, N. Han, Y. Jia, Q. Xie, X. Duan, T. Xie, X. Zheng, X. Sun and X. Duan, *Small*, 2018, **2**, 1800083.

18 Q. Wang and D. O'Hare, *Chem. Rev.*, 2012, **112**, 4124–4155.

19 K. Jin, H. Seo, T. Hayashi, M. Balamurugan, D. Jeong, Y. K. Go, J. S. Hong, K. H. Cho, H. Kakizaki, N. Bonnet-Mercier, M. G. Kim, S. H. Kim, R. Nakamura and K. T. Nam, *J. Am. Chem. Soc.*, 2017, **139**, 2277–2285.

20 K. R. Yang, A. J. Matula, G. Kwon, J. Hong, S. W. Sheehan, J. M. Thomsen, G. W. Brudvig, R. H. Crabtree, D. M. Tiede, L. X. Chen and V. S. Batista, *J. Am. Chem. Soc.*, 2016, **138**, 5511–5514.

21 N. C. Strandwitz, D. J. Comstock, R. L. Grimm, A. C. Nichols-Nielander, J. Elam and N. S. Lewis, *J. Phys. Chem. C*, 2013, **117**, 4931–4936.

22 L. C. Seitz, T. J. Hersbach, D. Nordlund and T. F. Jaramillo, *J. Phys. Chem. Lett.*, 2015, **6**, 4178–4183.

23 M. Huynh, C. Shi, S. J. Billinge and D. G. Nocera, *J. Am. Chem. Soc.*, 2015, **137**, 14887–14904.

24 Z. Morgan Chan, D. A. Kitchaev, J. Nelson Weker, C. Schnedermann, K. Lim, G. Ceder, W. Tumas, M. F. Toney and D. G. Nocera, *Proc. Natl. Acad. Sci. U. S. A.*, 2018, **115**, E5261–E5268.

25 T. Takashima, K. Hashimoto and R. Nakamura, *J. Am. Chem. Soc.*, 2012, **134**, 1519–1527.

26 K. Jin, A. Chu, J. Park, D. Jeong, S. E. Jerng, U. Sim, H. Y. Jeong, C. W. Lee, Y. S. Park, K. D. Yang, G. Kumar Pradhan, D. Kim, N. E. Sung, S. Hee Kim and K. T. Nam, *Sci. Rep.*, 2015, **5**, 10279.

27 C. Bae, T. A. Ho, H. Kim, S. Lee, S. Lim, M. Kim, H. Yoo, J. M. Montero-Moreno, J. H. Park and H. Shin, *Sci. Adv.*, 2017, **3**, e1602215.

28 M. Liu, X. Li, S. K. Karuturi, A. I. Tok and H. J. Fan, *Nanoscale*, 2012, **4**, 1522–1528.

29 S. Hu, M. R. Shaner, J. A. Beardslee, M. Lichterman, B. S. Brunschwig and N. S. Lewis, *Science*, 2014, **344**, 1005–1009.

30 A. C. Bronneberg, C. Höhn and R. van de Krol, *J. Phys. Chem. C*, 2017, **121**, 5531–5538.

31 T. Moehl, J. Suh, L. Severy, R. Wick-Joliat and S. D. Tilley, *ACS Appl. Mater. Interfaces*, 2017, **9**, 43614–43622.

32 L. Chen, J. Yang, S. Klaus, L. J. Lee, R. Woods-Robinson, J. Ma, Y. Lum, J. K. Cooper, F. M. Toma, L. W. Wang, I. D. Sharp, A. T. Bell and J. W. Ager, *J. Am. Chem. Soc.*, 2015, **137**, 9595–9603.

33 T. Yao, R. Chen, J. Li, J. Han, W. Qin, H. Wang, J. Shi, F. Fan and C. Li, *J. Am. Chem. Soc.*, 2016, **138**, 13664–13672.

34 G. Siddiqi, Z. Luo, Y. Xie, Z. Pan, Q. Zhu, J. A. Röhr, J. J. Cha and S. Hu, *ACS Appl. Mater. Interfaces*, 2018, **10**, 18805–18815.

35 B. B. Burton, F. H. Fabreguette and S. M. George, *Thin Solid Films*, 2009, **517**, 5658–5665.

This journal is © The Royal Society of Chemistry 2018

J. Mater. Chem. A, 2018, **6**, 21918–21926 | **21925**

36 F. Lyu, Y. Bai, Z. Li, W. Xu, Q. Wang, J. Mao, L. Wang, X. Zhang and Y. Yin, *Adv. Funct. Mater.*, 2017, **27**, 1702324.

37 M. B. Stevens, L. J. Enman, A. S. Batchellor, M. R. Cosby, A. E. Vise, C. D. M. Trang and S. W. Boettcher, *Chem. Mater.*, 2016, **29**, 120–140.

38 H. Xu, B. Wang, C. Shan, P. Xi, W. Liu and Y. Tang, *ACS Appl. Mater. Interfaces*, 2018, **10**, 6336–6345.

39 F. S. Zhang, J. W. Wang, J. Luo, R. R. Liu, Z. M. Zhang, C. T. He and T. B. Lu, *Chem. Sci.*, 2018, **9**, 1375–1384.

40 M. S. Burke, M. G. Kast, L. Trotochaud, A. M. Smith and S. W. Boettcher, *J. Am. Chem. Soc.*, 2015, **137**, 3638–3648.

41 H. Xiao, H. Shin and W. A. Goddard, *Proc. Natl. Acad. Sci. U. S. A.*, 2018, **115**, 5872–5877.

42 S. Hu, M. H. Richter, M. F. Lichterman, J. Beardslee, T. Mayer, B. S. Brunschwig and N. S. Lewis, *J. Phys. Chem. C*, 2016, **120**, 3117–3129.

43 J. Hu, C. Zhang, L. Jiang, H. Lin, Y. An, D. Zhou, M. K. H. Leung and S. Yang, *Joule*, 2017, **1**, 383–393.

44 J. K. Nørskov, J. Rossmeisl, A. Logadottir, L. Lindqvist, J. R. Kitchin, T. Bligaard and H. Jónsson, *J. Phys. Chem. B*, 2004, **108**, 17886–17892.

This journal is © The Royal Society of Chemistry 2018